Journal of Alloys and Compounds 489 (2010) 36–41

Contents lists available at ScienceDirect

Journal of Alloys and Compounds

journal homepage: www.elsevier.com/locate/jallcom

Thermodynamic analysis and synthesis of porous Mo_2C sponge by vapor-phase condensation and in situ carburization of MoO_3

S. Cetinkaya, S. Eroglu*

Istanbul University, Engineering Faculty, Department of Materials and Metallurgical Engineering, Avcilar, Istanbul, Turkey

ARTICLE INFO

Article history:
Received 20 August 2009
Accepted 9 September 2009
Available online 16 September 2009

Keywords:
Ceramics
Crystal growth
Gas-solid reactions
Vapor deposition
Thermodynamic modeling

ABSTRACT

Spongy porous MoO_3 deposits were grown by vaporization, vapor-phase transportation and condensation of MoO_3 in Ar flow. It was observed that increased source temperature (≥1200 K) and temperature gradient (≥100 K/cm) favor the formation of spongy deposit owing to high supersaturation of the oxide vapor at ~900 K. Spongy Mo_2C deposits consisting of intermingled platelet crystals with thin walls were synthesized by in situ carburization of the condensed MoO_3 using 0.05–0.1 mol of CH_4 and 1 mol of H_2 at 900 K. Thermodynamic analysis in the Mo–O–C–H system was used as a guide to predict the conditions for the formation of Mo_2C from the MoO_3–CH_4–H_2 reactants at 900 K. X-ray diffraction analysis showed that the carburized deposits consisted of single phase Mo_2C, in agreement with the thermodynamic prediction. The equilibrium analysis was also used to reveal possible reaction pathways to Mo_2C formation from MoO_3–CH_4–H_2 reactants which yielded gaseous products of H_2O, CO_2, CO, C_2H_6 and C_2H_4.

1. Introduction

Porous or foamed materials have received considerable attention for a variety of applications [1]. They are generally produced using powders with pore forming additives, spongy polymer templates infiltrated with slurries containing powders or by foaming of slurries. All these techniques involve removal of pore forming materials, which is a delicate and time consuming step carried out by leaching/thermal evaporation prior to sintering.

Porous ceramics have an important place in the field because they offer adequate strength and high permeability and are suitable for filtration of some metallic melts, incandescent gases, acids, alkalis and other corrosive media [2]. This type of material with whisker and platelet crystals is also used as a reinforcement component in the field of advanced composites with improved toughness [3]. For example, porous carbides are infiltrated with a matrix phase of low melting point metal, thus forming metal matrix–ceramic composite.

As a very important ceramic material, molybdenum carbide has been used widely because of its high melting point, high modulus, great hardness, high chemical stability and high catalytic activity. Molybdenum carbide powder is conventionally produced by powder metallurgical route [4]. Other methods now widely used for the synthesis of molybdenum carbide include solution route, sonochemical synthesis, alkalide reduction, temperature programmed carbothermal hydrogen reduction and chemical vapor deposition [5]. Among these methods, temperature programmed reaction between oxide precursors and a flowing mixture of hydrogen and carbon-containing gases has been an important one employed for the synthesis of molybdenum carbide particles which exhibit exceptionally high catalytic activity in hydrogen-involved reactions [6–10].

No report has been published on the synthesis of porous Mo_2C sponge with platelet-shaped crystals. In addition, detailed reaction mechanisms have not been reported in the literature for the formation of single phase Mo_2C from MoO_3–H_2–CH_4 mixtures. Hence, the objectives of this study were (a) to produce spongy Mo_2C by a vapor-phase condensation and in situ carburization of MoO_3 using H_2–CH_4 reactant gases and (b) to get a deeper insight into the thermochemistry of the process by equilibrium thermodynamic analysis.

2. Thermodynamic calculations

Thermodynamic analysis is a useful tool to predict the process parameters that yield the desired phases and to understand thermochemistry of material synthesis processes [11]. The analysis has been carried out by the method of minimization of the Gibbs' free energy of a system [12]. For a system of known input composition, it computes both the equilibrium gas phase and condensed phase compositions at a given pressure and temperature. The calculation requires specifying all possible species and condensed phases known to exist in the temperature range of interest. In the present study, MoO_3, CH_4 and H_2 were used as reactants for Mo_2C syn-

* Corresponding author. Tel.: +90 212 473 7065; fax: +90 212 473 7180.
E-mail addresses: seref@istanbul.edu.tr, serafettine63@gmail.com (S. Eroglu).

0925-8388/$ – see front matter © 2009 Elsevier B.V. All rights reserved.
doi:10.1016/j.jallcom.2009.09.053

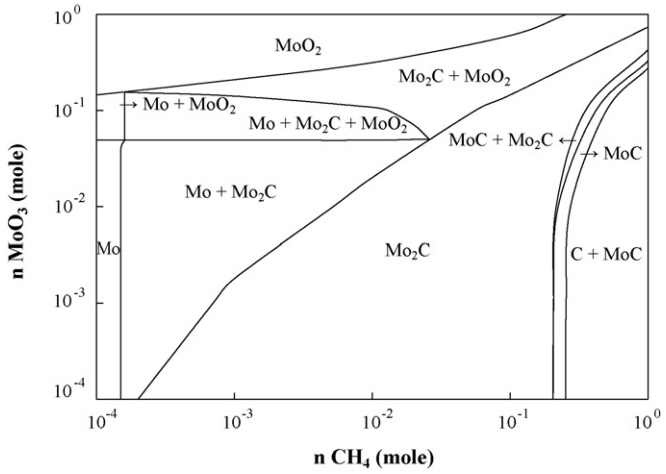

Fig. 1. Equilibrium stability diagrams depicting the condensed phases as a function of MoO_3 and CH_4 content in the Mo–O–C–H system for 1 mol of H_2 at 900 K.

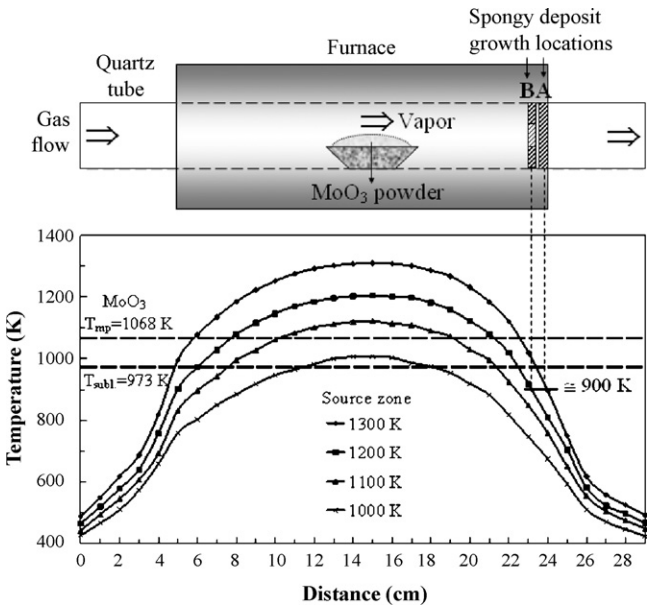

Fig. 2. Growth chamber, axial temperature profiles and locations for spongy deposit growth (designated as A and B) in the quartz tube at ~900 K. Horizontal lines represent sublimation and melting points of MoO_3.

thesis. Therefore, equilibrium calculations were carried out in the Mo–O–C–H system. In this system, 72 species were considered to be as the constituents of the gas phase. They include H_2, CH_4, CH_3, C_2H_4, C_2H_6, CH_2O, MoO, H_2O, CO, CO_2 and H_2MoO_4. Condensed equilibrium phases were assumed to be C, Mo, MoC, Mo_2C, MoO_2 and MoO_3. Input thermodynamic data in the form of Gibbs' free energy of the formation of the constituents were obtained from the thermochemical tables [13,14]. Thermodynamic calculations of complex equilibria were performed using a modified version of Eriksson's computer program SOLGASMIX [15]. The calculated results are shown in Fig. 1 as equilibrium stability diagram for the solid phases computed as a function of input reactant compositions of MoO_3 and CH_4, both in the range 10^{-4} to 1 mol at 1 mol of H_2 and at a temperature of 900 K. The selection of the amount of H_2 was based on the preliminary calculations which showed that 1 mol of H_2 prevents free-carbon formation for a very wide range of CH_4 and MoO_3 contents. The temperature of 900 K was chosen because condensation of spongy MoO_3 was observed at this temperature. Stable condensed phases are indicated on the diagram in Fig. 1. The boundaries in the diagram divide different domains in which the indicated phases are expected to form. As seen from Fig. 1, there are various phase fields including MoO_2, Mo, Mo + Mo_2C, Mo_2C + MoO_2, Mo_2C and C + MoC for the conditions studied. Mo_2C phase, which is the desired phase for the present work, is formed as single phase in a wide range of initial reactant contents of MoO_3 and CH_4. For the formation of single phase Mo_2C, the equilibrium calculations indicate generally that molar ratio of MoO_3 to CH_4 should be less than unity. Mo_2C phase field gets wider at low MoO_3 concentrations and at CH_4 concentrations <0.2 mol. Single Mo_2C formation range decreases with increasing MoO_3 content and is limited to narrow regions at high input MoO_3 and CH_4 reactant values. For example, for 1 mol of CH_4, single phase Mo_2C is formed at MoO_3 concentrations in the range ~0.4–0.7 mol. When the MoO_3/CH_4 ratio is <1 and CH_4 concentration is >0.2 mol, co-existence of MoC with Mo_2C, single phase MoC and formation of free C along with MoC phases are expected to form. In summary, the equilibrium calculations suggest that there is a wide range of the initial CH_4 and MoO_3 reactant contents to choose for the formation of single phase Mo_2C at 900 K and at 1 mol of H_2.

3. Experimental procedures

Using Fig. 1 as a guide, the initial compositions of the MoO_3–CH_4–H_2 reactant mixtures were chosen so as to synthesize the desired phase Mo_2C. It should be emphasized that capability of the experimental set-up (for example, the flow meter range, tube size) must also be considered for the selection. Therefore, the practical operating conditions were chosen such that the single phase Mo_2C is readily attainable in the reaction apparatus. For example, the MoO_3 amount of 10^{-4} mol is too small to characterize or to obtain the desired product while the MoO_3 content of 10^{-2} mol is too large for the reactor to be handled. Likewise, CH_4 content <10^{-2} mol is too small to be controlled by the flow meter used. Based on these considerations, the practical operating conditions are limited to the lower right side of the single Mo_2C phase field shown in Fig. 1. Hence, accessible initial reactant compositions were selected to be 10^{-3} mol of MoO_3, 0.05–0.1 mol of CH_4 and 1 mol of H_2 for the synthesis of single phase Mo_2C at 900 K.

The experimental set-up used for the present study essentially consists of a hot-wall furnace with SiC heating elements, a quartz tube (20 mm in diameter) and gas flow meters. The chemicals used were MoO_3 powder (Sigma–Aldrich), high purity argon (99.999%), methane (99.5 %) and hydrogen (99.99 %). The MoO_3 powder of ~0.001 mol (0.1440 g) in an alumina boat was placed at the hot zone of the furnace. The powders were vaporized on heating to the source temperatures of 1000, 1100, 1200 and 1300 K above the sublimation point (973 K) of MoO_3 at atmospheric pressure under high purity argon at a flow rate of 85 cm^3/min. When the source temperatures were reached, the reactive gases of CH_4 and H_2 were allowed to flow for 60 min at a rate of 20–40 cm^3/min and 370 cm^3/min which correspond to total amounts of ~0.05–0.1 mol of CH_4 and ~1 mol of H_2 admitted into the system, respectively. The reactive H_2 and CH_4 gases were pre-heated by passing through the hot zone in order to increase the decomposition of CH_4, which is known to be relatively stable at low temperatures such as 900 K. The deposits formed at the outlet side of the tube were removed from the tube. The morphologies were examined by a Scanning Electron Microscope (SEM). The deposits were crushed for phase analysis carried out by a parafocusing X-ray diffractometer equipped with a Cu radiation tube and a monochrometer. The crystallite size and microstrain were estimated from the X-ray diffraction peak profiles using the equation of

$$\frac{\beta\cos\theta}{\lambda} = \frac{1}{L} + \frac{4e\sin\theta}{\lambda} \quad (1)$$

where λ is the wavelength of Cu $K_{\alpha 1}$ radiation (0.154056 nm), θ is the diffraction angle, L is the crystallite size, e is the microstrain and β is the full breadth of a diffraction peak at half-maximum intensity. The breadth of the diffraction peaks was corrected for instrumental broadening (0.2°).

4. Results and discussion

4.1. Vaporization, condensation, in situ carburization and morphological analysis

The MoO_3 powders were vaporized on heating to the source temperatures of 1000, 1100, 1200 and 1300 K. The oxide vapor was physically transported by Ar flow to the colder side of the tube where condensation (crystal growth) took place. Fig. 2 shows the growth chamber, temperature profiles of the furnace and the

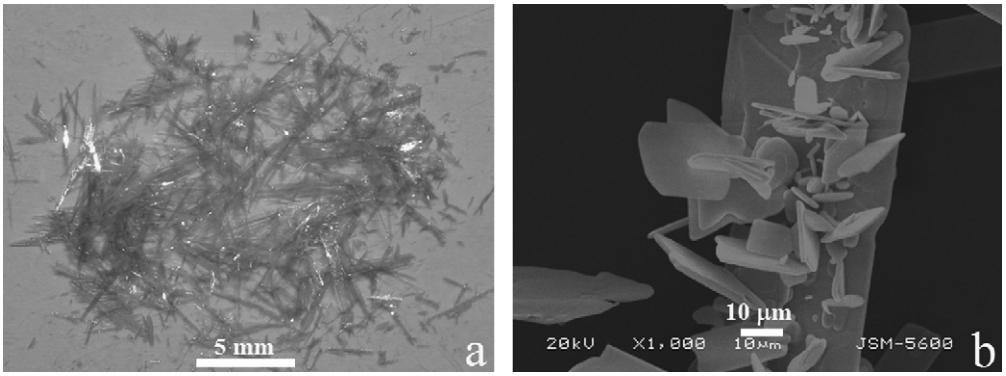

Fig. 3. (a) Macro view and (b) SEM image of the MoO_3 sponge condensed. Source and growth temperatures are 1300 and 900 K, respectively.

locations where spongy deposits were observed. During heating to 1300 K, it was observed that a large amount of deposit was grown radially covering the empty space across the tube (shown schematically at location A) at outlet side of the tube where the temperature was ~900 K (just below the sublimation point). The source temperature of 1200 K resulted in less amount of spongy deposit formed in circular-stripe shape (location B in the figure) at ~900 K. At 1000 and 1100 K, no marked spongy deposit was seen at ~900 K, but thin deposit condensed along the tube length. These results indicate that spongy deposit growth is related to source temperature, temperature profile (temperature gradient) and deposit growth temperature shown in Fig. 2. It is known that MoO_3 begins to sublime at 973 K, melts at 1068 K and vapor pressure increases noticeably above the melting point [16]. For example, equilibrium vapor pressures of MoO_3 at 900, 1000, 1100, 1200 and 1300 K are of the orders of 0.001, 1, 10, 100 and 300 torr, respectively [17]. It is obvious that oxide crystals grow when the vapor pressure (p) is higher than the equilibrium or saturated vapor pressure (p_e) at a given temperature. Condensation rate is proportional to the supersaturation ratio (p/p_e), which is the driving force for the crystal growth from the vapor-phase. When the source temperature is 1300 K, the driving force is the highest ($p/p_e \approx 300/10^{-3}$) at 900 K. Based on the vapor pressure data and the vaporization experiments, it can be deduced that on heating to 1300 K, highly supersaturated MoO_3 vapor and steep temperature gradient of 135 K/cm yielded rapid condensation of the vapor forming significant amount of spongy deposit across the tube at ~900 K. Similarly, at 1200 K, spongy deposit was observed at 900 K where the temperature gradient was 100 K/cm, but vapor pressure and temperature gradient were not sufficient to completely cover the cross-section of the tube (to fill the gap across the tube). At the source temperatures of 1100 and 1000 K, reduced temperature gradient (70 and 50 K/cm) and vapor pressure (low driving force) resulted in relatively uniform condensation over large axial distances. At 1000 K, some solid oxides were retained in the alumina boat indicating incomplete vaporization.

Fig. 3 shows macro and SEM images of the oxide condensed. As seen from the Fig. 3a, transparent and colorless MoO_3 spongy deposit with large platelet crystals formed from the vapor-phase at 900 K. The MoO_3 deposit growth was observed to be started from the tube wall and then, its growth continued perpendicular to the wall (radial growth), filling the empty space across the tube by forming a network of MoO_3 crystals. Rapid solid growth from a highly supersaturated MoO_3 vapor at 900 K led to spongy deposit. An interpenetrative structure displayed in the figure is likely to be formed owing to multiple nucleation and growth of crystals as seen in Fig. 3b.

After vapor-phase condensation, the CH_4 and H_2 gases were allowed to react with spongy oxide grown radially across the tube at the temperature of 900 K. It was observed that the reactive gases could pass through the oxide network of the deposit. Fig. 4a shows the dark gray spongy mass after in situ carburization, indicating that a transformation took place. Carburized deposits were observed to be mechanically stronger compared to the oxide one. After carburization, open porosity retained as the light could pass through the deposit. The thickness and diameter of the carburized deposit were measured to be ~3 mm and ~20 mm, respectively. SEM micrographs of the carburized deposits are shown in Fig. 4b–f. The morphology of the crystals at the periphery of the deposits consists of polyhedral grains bounded by crystallographic flat faces as seen from Fig. 4b. It seems that the spongy deposit starts to grow from these coarse grains formed on the tube wall. The morphologies at the inner sections of the deposits consist of thin platelet crystals with thickness typically in the range 90 nm–380 nm. Source temperatures (1200–1300 K) and reactant gas compositions studied do not appear to have noticeable effect on the morphologies as shown in Fig. 4c–f. Formation of platelet crystals with thin walls and the intermingled spongy Mo_2C deposit structure was attributed to successive branching and cracking of the oxide layers of MoO_6 octahedra held together by van der Waals forces during the phase transformation as a result of the transformation stress as can be seen in Fig. 4f. However, the exact growth mechanisms of the deposits are not clear and need to be further investigated.

4.2. Phase analysis

Fig. 5 displays X-ray diffraction patterns of the source oxide powder, the deposits before and after carburization along with the standard line diffraction patterns of the compounds published by JCPDS [18]. The MoO_3 source powder with orthorhombic crystal structure exhibited all the diffraction peaks reported in the corresponding standard (PDF no 05-0508) as expected. The X-ray diffraction pattern of the condensed oxide showed sharp peaks only from the $\{0\,k\,0\}$ planes of the orthorhombic crystal structure at diffraction angles of 25.6°, 38.85° and 67.40° corresponding to the (0 4 0), (0 6 0) and (0 1 0 0) crystal planes, respectively. Interplanar spacings (0.348, 0.232 and 0.139 nm) of these crystal planes were calculated to be in fairly good agreement with those (0.346, 0.231 and 0.139 nm) of the corresponding peaks of the standard MoO_3 powder diffraction file. The intensities of the $\{0\,k\,0\}$ peaks from the condensed oxide also agreed with those of the standard as shown in Fig. 5. These results indicate that anisotropic preferential crystal growth of $\{0\,k\,0\}$ crystallographic planes took place during condensation of the oxide as expected from large platelet-shaped crystals. XRD patterns (patterns e–g in Fig. 5) of the carburized deposits obtained at various synthesis conditions exhibited the peak characteristics of the hexagonal-closed packed Mo_2C in accordance with PDF no 35-0787. Interplanar spacings of the (1 0 0), (0 0 2), (1 0 1), (1 0 2), (1 1 0) and (1 0 3) crystal planes from the carburized deposits were calculated to be 0.2619, 0.2390, 0.2296, 0.1766, 0.1507 and 0.1356 nm, respectively. These values were found to be in good

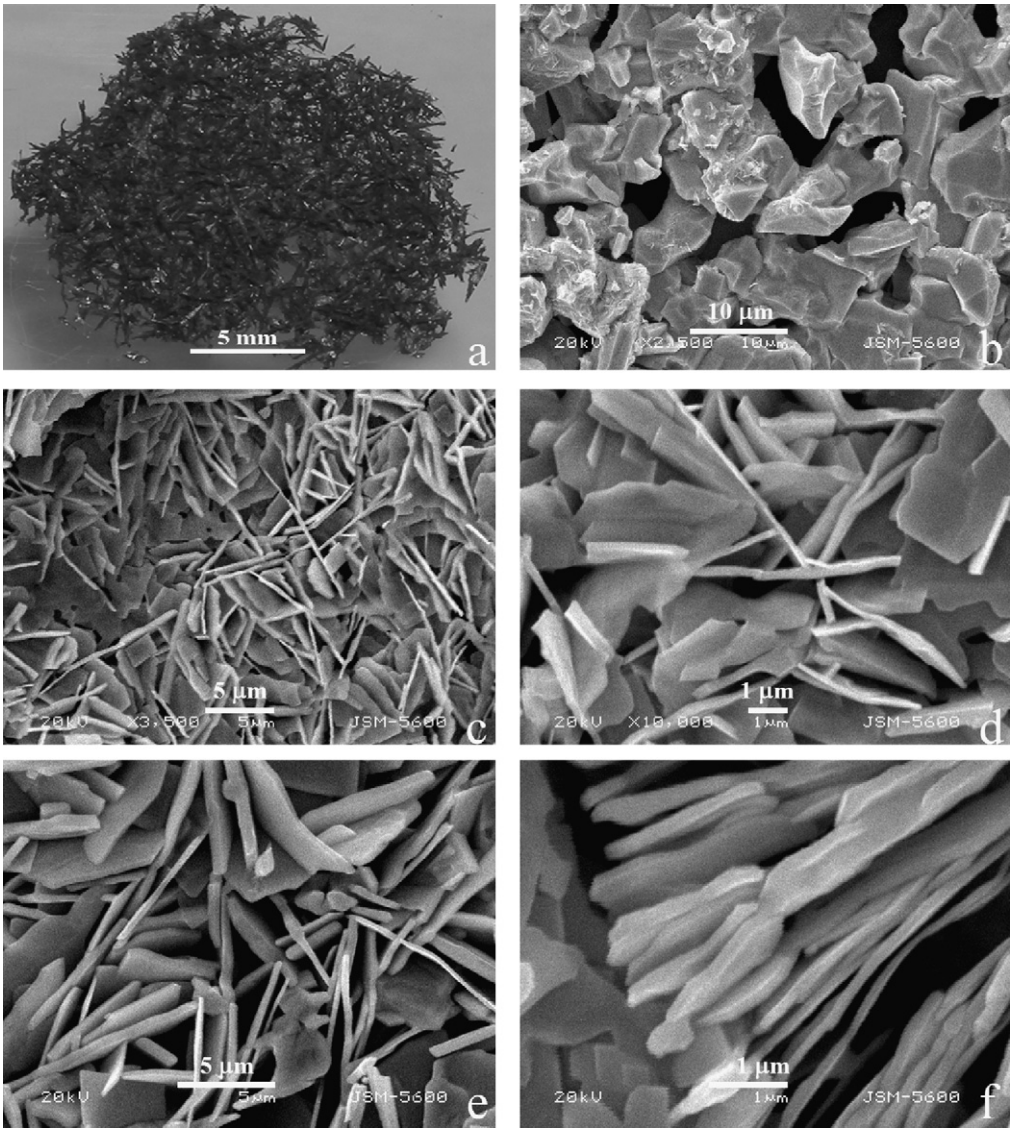

Fig. 4. (a) Macroview and (b–f) SEM images of the Mo_2C deposits obtained by the reaction of condensed oxide with H_2–CH_4 reactant mixtures. (b) Mo_2C crystals at the periphery and (c–f) inside of the deposit. The synthesis conditions are (a–d) 1300/900 K, H_2 (1 mol)–CH_4 (0.1 mol); (e) 1300/900K, H_2 (1 mol)–CH_4 (0.05 mol) and (f) 1200/900 K, H_2 (1 mol)–CH_4 (0.1 mol).

agreement with those (0.2608, 0.2367, 0.2286, 0.1753, 0.1506 and 0.1350 nm) of the standard powder diffraction file (PDF no 35-0787). The observed intensities were also in fairly good agreement with those of the standard as seen in Fig. 5. No free-carbon or molybdenum oxide in the carburized deposits was detected by XRD. This result is in agreement with the thermodynamic predictions for the experimental conditions investigated. The patterns from the carburized samples showed broad diffraction peaks which were attributed to microstrain and small crystallite size. The microstrain and crystallite or domain size estimated using Eq. (1) were typically ~0.5 % and ~90 nm, respectively. Microstrain is developed in the deposit during transformation from orthorhombic oxide to hexagonal carbide. It is believed that coherent X-ray diffraction comes from small crystallites or domains in the platelet crystals, which were not observable in the SEM micrographs.

4.3. Thermodynamic modeling of reaction pathways to Mo_2C formation

Using the thermodynamic calculations in the Mo–C–O–H system as a guide, single phase Mo_2C was successfully produced at

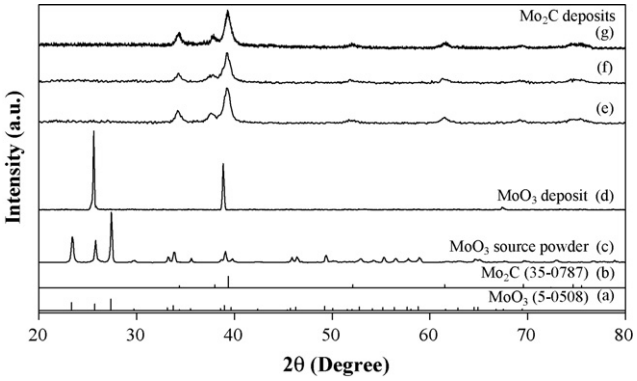

Fig. 5. X-ray diffraction patterns of (a) the standard MoO_3 (PDF no 5-0508), (b) standard Mo_2C (PDF no 35-0787), (c) MoO_3 source powder, (d) condensed oxide and (e–g) carburized deposits. The synthesis conditions are (d) 1300/900 K, (e) 1200/900 K, H_2 (1 mol)–CH_4 (0.1 mol), (f) 1300/900 K, H_2 (1 mol)–CH_4 (0.05 mol) and (g) 1300/900 K, H_2 (1 mol)–CH_4 (0.1 mol).

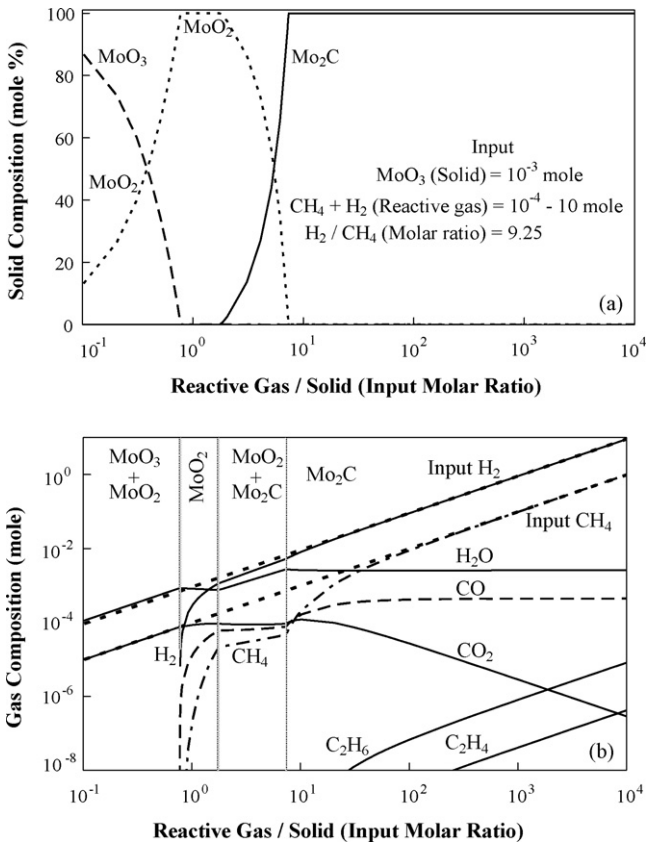

Fig. 6. Variations of (a) equilibrium solid and (b) gas product compositions with initial reactant gas ($CH_4 + H_2$)/solid (MoO_3) molar ratio at 900 K. Two parallel inclined lines represent the input values for H_2 and CH_4. Solid-phase fields are seperated by vertical lines in (b).

the initial reactant compositions of 0.001 mol MoO_3, 0.05–0.1 mol CH_4 and 1 mol H_2. Further analysis was carried out in order to simulate the process thermodynamically and to reveal reaction pathways by varying input reactant gas ($H_2 + CH_4$)/solid (MoO_3) ratio. Total amount of reactant gas was varied in the range of 10^{-4} to 10 mol. The amount of solid MoO_3 and the H_2/CH_4 molar ratio were fixed at 10^{-3} mol and 9.25, respectively. This gives reactant gas/solid molar ratios varying from 10^{-1} (excessive MoO_3) to 10^4 (excessive gas). Excessive solid MoO_3 and excessive reactant gas conditions may simulate early and final stages of carburization reaction where total amount of reactant gas admitted into system is low and high, respectively. From experimental point of view, since flow rate of gaseous reactants are constant, initial stages for Mo_2C formation may correspond to short reaction times and vice versa. At each gas/solid ratio, the amounts of equilibrium solid phases and gaseous product species formed in the process were determined. The results are plotted in Fig. 6 showing the effect of input reactant gas/solid ratio on the equilibrium solid-phase and gas phase compositions. It is seen from Fig. 6a, there are four phase fields present at molar ratios in the range of 10^{-1} to 10^4. As the gas/solid ratio increases, $MoO_3 + MoO_2$, MoO_2, $MoO_2 + Mo_2C$ and Mo_2C phase fields are formed successively. At the gas/solid ratios <0.8, MoO_3 is reduced to MoO_2 and the amount of MoO_3 decreases with increasing reactant gas. At ratios in the range of 0.8–1.8, single phase MoO_2 exists. Above >1.8, MoO_2 starts to transform to Mo_2C and Mo_2C content increases. Above ~7.5, single phase of Mo_2C forms and the yield of Mo_2C formation with respect to MoO_3 becomes 100 % for the conditions studied. From the above analysis, it is deduced that Mo_2C formation follows the path $MoO_3 \rightarrow MoO_2 \rightarrow Mo_2C$ with increasing amount of reactant gas/solid ratio showing that metallic molybdenum and free-carbon are not involved in the formation of Mo_2C. These results are in agreement with the works carried out on synthesis of Mo_2C catalyst particles using MoO_3–CH_4–H_2 mixtures [7,10].

In order to gain more insight into thermochemistry of the process, the changes in composition of solid and the gas phases were studied as input reactant gas/solid ratio varied. Hence, possible chemical reaction mechanisms could be suggested using the equilibrium concentrations of products and reactants. Fig. 6b shows changes in the concentration of the gaseous products with the input reactant gas/solid molar ratio. As seen from the figure, the major gaseous product species are formed to be H_2O, CO and CO_2 whose amounts vary with input gas/solid ratio. As also seen in Fig. 6b, the product H_2O gas is by far the dominant gaseous specie at all gas/solid ratios under the conditions considered by this diagram. The concentration of CO_2 is calculated to be higher than that of CO at ratios <8. At higher gas/solid ratios, the concentration of CO becomes higher. Minor C_2H_4 and C_2H_6 species are seen at high gas/solid ratios. These results are in qualitative agreement with the gaseous product species determined experimentally during the Mo_2C catalyst particle synthesis using the same input reactants [7–9]. At $MoO_2 + MoO_3$ phase field (indicated by vertical lines in Fig. 6b), where excessive MoO_3 is present, major gaseous product species are formed to be CO_2 and H_2O whose amounts increase with reactant gas up to a ratio of 0.8 at which transformation MoO_3 to MoO_2 is completed. H_2 and CH_4 are not present in the gas phase at gas/solid ratios <0.8. As shown in the Fig. 6b, all H_2 and CH_4 reactants are predicted to be consumed through the formation of H_2O and CO_2. This result may suggest that the formation of MoO_2 from MoO_3 takes place via the following reactions:

$$MoO_3 + H_2 \rightarrow MoO_2 + H_2O \quad (\Delta G_r^\circ = -103,105\,J) \tag{2}$$

$$4MoO_3 + CH_4 \rightarrow 4MoO_2 + 2H_2O + CO_2 \quad (\Delta G_r^\circ = -420,618\,J) \tag{3}$$

where ΔG_r° is the standard Gibbs' free energy change of the reactions. Eq. (3) indicates that CH_4 acts as a reducing agent as well. MoO_2 is predicted to form by the following net reaction which may be viewed as the total reaction of (2) and (3):

$$5MoO_3 + H_2 + CH_4 \rightarrow 5MoO_2 + 3H_2O + CO_2 \quad (\Delta G_r^\circ = -523,723\,J) \tag{4}$$

At single phase MoO_2 region, a slight decrease in H_2O and a slight increase in CO_2 content can be seen in Fig. 6b. H_2 and CH_4 concentrations increase with initial gas/solid ratio mostly owing to excessive $H_2 + CH_4$ reactants. At single MoO_2 phase field, a new product specie of CO forms with increasing amount. Possible CO formation reactions may be suggested as follows:

$$4MoO_3 + CH_4 + H_2 \rightarrow 4MoO_2 + CO + 3H_2O \quad (\Delta G_r^\circ = -414,369\,J) \tag{5}$$

$$CH_4 + H_2O \rightarrow CO + 3H_2 \quad (\Delta G_r^\circ = -1,949\,J) \tag{6}$$

Eq. (5) shows that the reaction between methane and MoO_3 in the presence of hydrogen leads to solid MoO_2, gaseous CO and H_2O species. Eq. (6) may be viewed as homogeneous gas phase reaction between methane and water produced by the reduction of oxide. At the $MoO_2 + Mo_2C$ phase field, CO_2 content essentially remains constant, but the amount of H_2O increases. A slight increase in CO content is also seen. The amount of Mo_2C phase increases and MoO_2 content decreases with increasing input gas concentration in this region (Fig. 6a). Based on these results, the formation of Mo_2C from MoO_2 may be presented with the following reactions:

$$2MoO_2 + 2H_2 + CH_4 \rightarrow Mo_2C + 4H_2O \quad (\Delta G_r^\circ = -12,753\,J) \tag{7}$$

In the single phase Mo_2C domain, the major gaseous specie H_2O reaches the highest level as shown in Fig. 6b. Among the carbon-bearing product gases, CO is seen to have the highest concentration in this field. The gaseous specie of CO_2 has lower concentration than that of CO and its amount decreases with increasing input gas/solid ratio. The above studies suggest that the carburization of MoO_3 by methane in the presence of hydrogen includes two successive steps: (a) reduction of the MoO_3 to MoO_2 by H_2–CH_4 mixture and (b) reaction between partially reduced oxide and H_2–CH_4 mixture. These results indicate that several total reactions between the input reactants to produce Mo_2C are expected to occur. The reactions are suggested as follows:

$$2MoO_3 + CH_4 + 4H_2 \rightarrow Mo_2C + 6H_2O \quad (\Delta G_r^\circ = -218,963\,J) \quad (8)$$

$$2MoO_3 + 2CH_4 + H_2 \rightarrow Mo_2C + CO + 5H_2O \quad (\Delta G_r^\circ = -220,912\,J) \quad (9)$$

$$2MoO_3 + 7/5CH_4 + 12/5H_2 \rightarrow Mo_2C + 2/5CO_2 + 26/5H_2O \quad (\Delta G_r^\circ = -222,242\,J) \quad (10)$$

$$2MoO_3 + 3CH_4 + 3H_2 \rightarrow Mo_2C + C_2H_6 + 6H_2O \quad (\Delta G_r^\circ = -148,111\,J) \quad (11)$$

$$2MoO_3 + 3CH_4 + 2H_2 \rightarrow Mo_2C + C_2H_4 + 6H_2O \quad (\Delta G_r^\circ = -125,113\,J) \quad (12)$$

At gas/solid ratios >7.5 (in the single Mo_2C phase domain), reactions (8–10) may be considered as the dominant net reactions (the most important ones) represent the equilibrium between the input reactants (MoO_3–CH_4–H_2) and the products (solid Mo_2C and the most abundant species H_2O, CO and CO_2). The reactions (11) and (12) may be viewed as side reactions in the single Mo_2C phase field.

5. Conclusions

Spongy MoO_3 with preferential growth of $\{0\,k\,0\}$ crystal planes was deposited by vaporization, vapor transportation and condensation of the oxide powder at 900 K in Ar flow. When the source temperature of 1300 K was used, complete coverage of the tube cross-section with MoO_3 deposit was obtained under a high temperature gradient of 135 K/cm owing to large supersaturation of the oxide vapor at 900 K. Spongy Mo_2C deposits with thin platelet crystals were synthesized by in situ carburization of MoO_3 condensed using H_2 (1 mol)–CH_4 (0.05–0.1 mol) reactant mixtures at 900 K. Equilibrium calculations based on the minimization of Gibbs' free energy in the Mo–O–C–H system were used to determine the input reactant concentrations (0.001 mol of MoO_3, 1 mol of H_2 and 0.05–0.1 mol of CH_4) that yielded single phase Mo_2C at 900 K. XRD phase analysis on the products revealed that the experimental results were in agreement with the thermodynamic prediction. Thermodynamic analysis also suggests that the formation of Mo_2C takes place by reduction of MoO_3 to MoO_2 followed by carburization. It was shown that reactions pathways to the formation of Mo_2C from the input MoO_3–CH_4–H_2 reactants could be proposed using equilibrium thermodynamic analysis.

Acknowledgements

This work was supported by Research Fund of the Istanbul University, project number 1453. It was partially based on a Ph. D. thesis pursued by S.C.

References

[1] M. Nanko, H. Onishi, K. Ishizaki, Ceram. Ind. (1996) 331–337.
[2] V.M. Sleptsov, E.M. Prshedromirskaya, Y.P. Kukota, Powder Metall. Metal. Ceram. 4 (1965) 849–853.
[3] R.W. Rice, Ceramic Fabrication Technology, Taylor and Francis Group, Routledge, 2002.
[4] P. Schwarzkopf, R. Kieffer, Refractory Hard Metals, The Macmillan Company, New York, 1953.
[5] M. Patel, J. Subrahmanyam, Mater. Res. Bull. 43 (2008) 2036–2041.
[6] Q. Zhu, Q. Chen, X. Yang, D. Ke, Mater. Lett. 61 (2007) 5173–5174.
[7] A. Hanif, T. Xiao, A.P.E. York, J. Sloan, M.L.H. Green, Chem. Mater. 14 (2002) 1009–1015.
[8] K.T. Jung, W.B. Kim, C.H. Rhee, J.S. Lee, Chem. Mater. 16 (2004) 307–314.
[9] S. Li, W.B. Kim, J.S. Lee, Chem. Mater. 10 (1998) 1853–1862.
[10] J. Patt, D.J. Moon, C. Phillips, L. Thompson, Catal. Lett. 65 (2000) 193–195.
[11] S. Eroglu, S.C. Zhang, G.L. Messing, J. Mater. Res. 11 (1996) 2131–2134.
[12] G. Eriksson, Chem. Scr. 8 (1975) 100–103.
[13] M.W. Chase, C.A. Davies, J.R. Downey, D. J. Frurip, R.A. McDonald, A.N. Syverud, JANAF Thermochemical Tables, third ed., J. Phys. Chem. Ref. Data 14 (Suppl. l) (1985).
[14] I. Barin, Thermochemical Data of Pure Substances, VCH Verlagsgesellschaft, WeinHeim, 1993.
[15] T.M. Besmannn, SOLGASMIX-PV, A Computer Program to Calculate Equilibrium Relationships in Complex Chemical Systems. Oak Ridge National Laboratory, Report No. ORNL/TM-5775, 1977.
[16] F.F. Habashi, Handbook of Extractive Metallurgy III, Wiley-VCH, Heidelberg, 1997.
[17] W.H. Kohl, Handbook of Materials and Techniques for Vacuum Devices, American Institute of Physics, New York, 1995.
[18] JCPDS, International Center for Diffraction Data. Swartmore PA, 2008.